RESEARCH ARTICLE | DECEMBER 24 2024

The impact of electron inertia on collisional laser absorption for high energy density plasmas

Special Collection: Papers from the 66th Annual Meeting of the APS Division of Plasma Physics

James R. Young ; Pierre-Alexandre Gourdain

Phys. Plasmas 31, 123904 (2024)
https://doi.org/10.1063/5.0237787

The impact of electron inertia on collisional laser absorption for high energy density plasmas

Cite as: Phys. Plasmas **31**, 123904 (2024); doi: 10.1063/5.0237787
Submitted: 6 September 2024 · Accepted: 25 November 2024 ·
Published Online: 24 December 2024

James R. Young[1,2,a)] and Pierre-Alexandre Gourdain[1,2]

AFFILIATIONS

[1]Department of Physics and Astronomy, University of Rochester, Rochester, New York 14627, USA
[2]Laboratory for Laser Energetics, University of Rochester, Rochester, New York 14627, USA

Note: This paper is part of the Special Collection: Papers from the 66th Annual Meeting of the APS Division of Plasma Physics.
Note: Paper TI3 3, Bull. Am. Phys. Soc. **69** (2024).
[a)]Invited speaker. **Author to whom correspondence should be addressed:** jyoung36@ur.rochester.edu

ABSTRACT

High-power lasers are at the forefront of science in many domains. While their fields are still far from reaching the Schwinger limit, they have been used in extreme regimes, to successfully accelerate particles at high energies, or to reproduce phenomena observed in astrophysical settings. However, our understanding of laser–plasma interactions is limited by numerical simulations, which are very expensive to run as short temporal and spatial scales need to be resolved explicitly. Under such circumstances, a non-collisional approach to model laser–plasma interactions becomes numerically expensive. Even a collisional approach, modeling the electrons and ions as independent fluids, is slow in practice. In both cases, the limitation comes from a direct computation of electron motion. In this work, we show how the generalized Ohm's law captures collisional absorption phenomena through the macroscopic interactions of laser fields, electron flows, and ion dynamics. This approach replicates several features usually associated with explicit electron motion, such as cutoff density, reflection, and absorption. As the electron dynamics are now solved implicitly, the spatial and temporal scales of this model fit well between multi-fluid and standard magneto-hydrodynamics scales, enabling the study of a new class of problems that would be too expensive to solve numerically with other methods.

INTRODUCTION

Laser–plasma interactions (LPIs) are key features when a high-power laser drives materials into ionized states. For example, stimulated Brillouin[1] combined with ponderomotively driven plasma response has long been a major concern for inertial confinement fusion (ICF),[2,3] especially when cross-beam energy transfer (CBET)[4,5] is involved. In addition to providing a source of magnetization in plasmas,[6,7] the very nature of LPIs can change in the presence of strong magnetic fields,[8] like those generated around magnetars[9] and white-dwarves,[10] and prior research even links fast radio bursts in the relativistic winds of magnetars[11,12] to ponderomotive self-focusing of electromagnetic radiation.[13,14] LPI can also cause electron and ion density modulations that grow and steepen[15–17] and whose sharp nature has been recently used to form plasma gratings[18–20] for high-power plasma optics. The gratings can be produced through ionization effects of overlapping laser beams[21–23] or ponderomotively driven ion and electron peaks.[19,24,25] The former requires models capable of handling not only ionization but also the effect of the laser on the newly formed under-dense plasma, while the latter requires resolving electron effects on the ion scale. For this work, we focus on collisional absorption, which is the primary ingredient of inverse bremsstrahlung (IB)[1,26] and is the most fundamental laser–plasma interaction.

In one regime, when the ions are mostly frozen in place, a common situation in laser wakefield acceleration simulations, particle-in-cell (PIC) models[27] capture LPIs extremely well. In the other regime, when the ion and electron motion is ambipolar, the essence of LPIs is deeply rooted in IB, where ray-tracing (RT)[28,29] can be used to track the energy budget left inside the electric field as the laser beam travels inside the plasma. This model rests on the application of WKB approximation, which assumes the electron density varies slowly enough to have a well-defined wave-vector and frequency. While the first approach is typically collisionless (although collisional models have been successfully added[30–36]) and uses the Vlasov approximation, the second is collisional and uses conservation laws to track the ion dynamics.[37] State-of-the-art MHD codes (e.g., *FLASH*,[38] *LILAC*,[39] *DRACO*,[40] and *HYDRA*[41]) often drop some or all of these electron

terms. They split the LPI into a radiation component (eikonal approximation of the laser field) and an absorption component (i.e., IB), while only coupling electrons and rays via the plasma dispersion relation.[42] Unfortunately, problems that fall in between regimes are more difficult to model. Hybrid codes[43] have been used recently to bridge this scale gap, running a multi-fluid approximation when possible and switching to a kinetic one when the fluid approach breaks down.

However, when LPIs occur in a fully formed plasma,[44] such as those produced in modern pulsed-power machines,[45–48] the ray approximation usually breaks down. The large density gradients and complex geometrical structures present before the laser is fired will generate situations where the paraxial assumption is violated and ray-tracing cannot be used. Additionally, ray-tracing does not inherently include interactions between rays, which is necessary to model more complex LPI, such as CBET. Additional models must be used to allow ray interactions.[49,50] Resonant absorption for p-polarized light is not natively captured by ray tracing and requires analytic asymptotic solutions for the absorption coefficients.[51] For hot electron temperatures and large spatial density gradients, this can reduce the collisional (or Landau) damping by as much as 50%,[52] which makes this an important subject for ICF.[53,54]

Up to now, such situations relied on blending multiple computational approaches to study these regimes.[55,56] This paper shows that the physics necessary to capture collisional LPI is fully accounted for in the extended magnetohydrodynamics (XMHD) model, where electron terms have been retained in the generalized Ohm's law (GOL). The algorithms originally developed for the XMHD code PERSEUS[57,58] are capable of capturing LPI natively with only minor modifications to appropriately account for transport coefficients, such as resistivity and thermal heat conduction. The dimensional parameters for the code also need to be adjusted for this new laser regime, which will be discussed in section "The Generalized Ohm's Law Scaled for Laser–Plasma Interactions."

Although this XMHD model advances its equations explicitly in their fluxes, there is an additional local semi-implicit advance of **E** and **j** in GOL and Maxwell–Ampère's law, which enables modeling of the electron physics without needing a CPU-intensive global solve. While this semi-implicit correction allows for large time-steps in a typical MHD regime, here, we still need to resolve the laser wavelength. For high resolution and small timesteps, the semi-implicit method reduces to an explicit scheme. However, once the laser leaves the simulation, it is possible to revert to lower resolution and larger timesteps while retaining electron effects. More details of this algorithm can be found in the original paper[57] and thesis[58] from which it is built.

Since correctly capturing IB only relies on collisional LPI, then at least for low-energy lasers, the primary energy delivery mechanism is natively present. We expect this to transition away from IB when the laser power is increased, which will require additional forms of LPI. While we restrict our discussion to non-relativistic plasma interaction using high power (i.e., long pulse) lasers, this framework can be extended to relativistic plasmas by modifying the conservation laws and the GOL.[59]

The first section of this paper uses dimensional analysis to show which terms in the GOL are important to LPIs in the XMHD framework. Then, we show quantitatively how XMHD handles LPIs in slab geometries using PERSEUS.[57,58] Finally, we highlight how energy transfers from the laser field to the plasma.

THE GENERALIZED OHM'S LAW SCALED FOR LASER–PLASMA INTERACTIONS

Redimensionalization of the generalized Ohm's law using LPI characteristic scales

Dimensional analysis comes into play to make important parameters appear in XMHD equations.[57] Removing all units in conservation laws and Maxwell's equation can be done with taking three independent characteristics scales, such as time t_0, speed v_0, and mass density ρ_0.[60] One key step is necessary to arrive to a self-consistent result. Conservation of momentum dictates that the characteristic speed v_0 should also be the characteristic Alfvén speed. In the framework of laser–plasma interactions, we can take the electromagnetic wave speed c as our characteristic speed, $v_0 = c$. Following Faraday's law, we relate the electric and magnetic fields characteristic scales as $E_0 = cB_0$. As we remove dimensions from each XMHD equation, we find the following relationships between the different characteristic scales: the thermal pressure scale is $p_0 = \rho_0 c^2$, the resistivity scale $\eta_0 = t_0/\varepsilon_0$, the magnetic field scale is $B_0 = \sqrt{\rho_0/\varepsilon_0}$, and the current density scale is $j_0 = \sqrt{\rho_0/\mu_0}/t_0$.

We assume here quasi-neutrality and separate electron and ion energies. However, the electron momentum is computed implicitly, using the time evolution of the electrical current density via the GOL, given by

$$\begin{aligned}\mathbf{E} = &-\mathbf{v}\times\mathbf{B} + \eta\mathbf{j} + \frac{1}{\omega_{pe}t_0}\sqrt{\frac{m}{n_e}}(\mathbf{j}\times\mathbf{B} - \vec{\nabla}p_e)\\ &+\left(\frac{1}{\omega_{pe}t_0}\right)^2\left(\frac{\partial\mathbf{j}}{\partial t} + \vec{\nabla}\cdot(\mathbf{vj}+\mathbf{jv})\right)\\ &-\left(\frac{1}{\omega_{pe}t_0}\right)^3\sqrt{mn_e}\,\vec{\nabla}\cdot\left(\frac{1}{n_e}\mathbf{jj}\right).\end{aligned} \tag{1}$$

Here, **E** is the electric field, **v** is the flow speed, **B** is the magnetic field, **j** is the current density, n_e is the electron number density, m is the ratio of the ion mass to the electron mass, ρ is the mass density, p is the thermal pressure, and η is the electric resistivity, *all dimensionless*.

The dimensional electron plasma frequency $\omega_{pe} = \sqrt{N_e e^2/(m_e\varepsilon_0)}$ is highlighted by the nondimensionalization process. Furthermore, N_e is electron number density, e is the elementary charge, and m_e is the electron mass, *all dimensional*. It is now in front of all the terms connected to electron physics inside Eq. (1).

Characterization of LPIs in XMHD

To understand what type of LPI takes place in XMHD, we can look at the interaction of a plane electromagnetic wave traveling to the left with a plasma slab located in the region $x < 0$. At early times, the ion fluid is static and has no spatial dependence in the region $x < 0$. We can equate the laser electric field at the plasma–vacuum interface, the LHS of Eq. (1), to the electric field inside the plasma, the RHS of Eq. (1). In this case, Eq. (1) simplifies to

$$\mathbf{E} \approx \eta\mathbf{j} + \frac{1}{\omega_{pe}^2 t_0^2}\frac{\partial\mathbf{j}}{\partial t}, \tag{2}$$

dropping the third order terms in $1/\omega_{pe}t_0$ since the characteristic timescale of the interaction t_0 is much larger than the electron timescale (i.e., $1/\omega_{pe}$). In other terms, we look at effects that are much

slower than the electron plasma frequency. At this early point in time, the ions have not moved yet and the Lorentz force equilibrates exactly the electron pressure gradient. And so we also drop the first order term in $1/\omega_{pe}t_0$, since

$$\mathbf{j} \times \mathbf{B} = \vec{\nabla} p_e, \tag{3}$$

from the momentum equation.

Modifying Maxwell–Ampère's law using Eq. (2) while taking η and ω_{pe} to have small time variations compared to t_0, we get

$$\frac{1}{\omega_{pe}^2 t_0^2}\frac{\partial^2 \mathbf{j}}{\partial t^2} + \eta\frac{\partial \mathbf{j}}{\partial t} + \mathbf{j} \approx \nabla \times \mathbf{B}. \tag{4}$$

Equation (4) is the equation of a damped harmonic oscillator with a resonant frequency, ω_{pe}, driven by the curl of the laser magnetic field **B**.

The dimensional analysis shows that LPIs are mediated by electron inertia and Maxwell–Ampère's law in XMHD. So, the laser energy is transferred to the electron fluid via harmonic oscillation. This is possible because we can now store mechanical energy inside the electron fluid, a transformation that requires the electrons having mass (hence inertia). Resonance allows this energy to become large enough so it can interact non-linearly with the incoming electromagnetic wave. Consequently, XMHD recovers some common features found in the two-fluid models,[37,61] while resolving the electron motion on the ion timescale only. We refer the reader to prior work[44,57] to see a complete set of equations being solved in the code.

Although electron inertia has been important in studies of collisionless magnetic reconnection,[62–65] often the components are broken to include only the convective acceleration term $(\mathbf{v_e} \cdot \nabla \mathbf{j})$ rather than considering temporal variations of current directly,[66] which are key to absorption and eventual collisional dissipation.

VALIDATION OF XMHD SIMULATIONS USING PARTICLE-IN-CELL AND RAY-TRACING

First, we demonstrate this model is consistent with ray-tracing. Furthermore, XMHD simulations show almost perfect agreement with OSIRIS[67] for a duration of at least 3 orders of magnitude larger than the laser period. For the XMHD simulations, a non-relativistic (normalized vector potential $a_o < 0.01$) s-polarized laser was propagated into a simulation domain by setting an oscillatory electromagnetic field as a boundary condition. The magnetic field component, B_y, was defined on the vertical boundary so the Poynting flux was directed to the left. The beam has a uniform spatial profile, $B_y = B_{max}\cos(kx + \omega t)$. Here, $E_{max} = \sqrt{2I_{laser}/(c\epsilon_0)}$, $k = 2\pi/\lambda$, and $\omega = ck$ with I_{laser} varying from $10^{16} \rightarrow 10^{18}\mathrm{Wm}^{-2}$ $(a_0 \approx 0.001 \rightarrow 0.01)$ and $\lambda = 527$ nm. The PIC simulation uses identical geometry and laser characteristics. For ray-tracing, we specifically use a ramp density profile from $n_e/n_{crit} = 0 \rightarrow 1.0$. All simulations other than the RT comparison in Fig. 1 are performed in a 2D pencil domain (9 cells in the y-direction and the rest of the resolution in the x-direction). To see a fully 2D simulation of LPI, then we refer the reader to prior work.[44] The thermal conduction model is a simple cross-over hybrid of magnetized and unmagnetized formulas[37] and is applied to both ions and electrons.

Ray-tracing

Figure 1 shows rays as green arrows overlaying the XMHD simulation for an s-polarized laser propagating toward the density ramp.

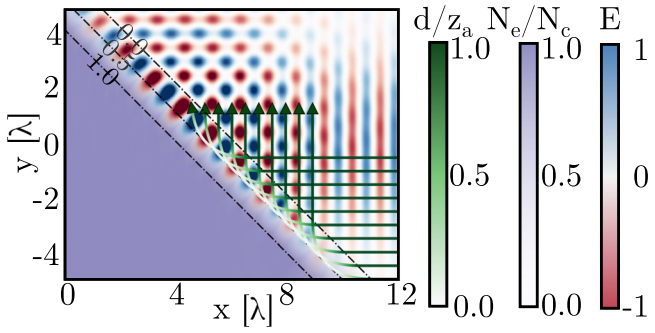

FIG. 1. A plot of a 45° ramp electron density profile with S-polarized light coming from $x = 12\lambda$ with $I_{laser} = 3.5 \times 10^{17}\mathrm{W/m^2}$ and $\lambda = 527$ nm. Overlaid on this are 10 ray-traced solutions for this same density profile that are colored based on their distances from the turning point in units of Airy skin depth, z_a.

The WKB approximation assumes the turning point should occur when $n_e/n_{crit} = \cos^2(\theta)$, which for this geometry $(\theta = 45°)$ is $n_e/n_{crit} = 0.5$. The color of the green ray shows the distance of the ray from the theoretical turning point in units of Airy skin depth (z_a), within which the WKB approximation is no longer valid.[52] We see that within one z_a, the light becomes evanescent and decays to zero. For s-polarized light, there is no resonant absorption and the total deposited energy is equivalent to ray-tracing approximation. However, this will no longer be true for p-polarized light.

Particle-in-cell

Although collisions are not a native part of the PIC algorithm, the *Monte Carlo binary collision* model (BCM), introduced by Takizuka and Abe in 1977,[30] successfully incorporated them into PIC codes by updating velocities of particle pairs within spatial cells where plasma properties changed slowly. This method was extended to relativistic plasmas,[31] but typically works with mesh sizes smaller than the lengths of the density and temperature gradients.[32] Unfortunately, these types of methods require somewhat limiting time steps shorter than the mean collision time.

Grid-based methods address some of the limitations of BCMs. One approach generates a "field particle" from a sampled grid velocity distribution, which collides with real test particles.[36] While these methods often lack native energy conservation and require post-processing, recent advances have developed energy-conserving models, albeit with increased field solver complexity.[68] Notably, grid-based methods show a remarkable improvement in time step constraints and are typically compatible with hybrid fluid-kinetic systems as they work by sampling field particles from velocity distribution moments typically evolved by fluid codes.[36]

Recently, cumulative scattering models based on BCMs, such as the Nanbu–Yonemura method,[33] improved computational efficiency by grouping small-angle collisions into a single effective event. These algorithms were later updated to address errors when PIC macro-particles have different weights[35] and were also extended to relativistic cases,[34] which is the model used in the OSIRIS simulations we now present in this work.

Figure 2 shows n_e/n_{crit} and current density, j, for equivalent initializations and boundary conditions for both PIC and XMHD

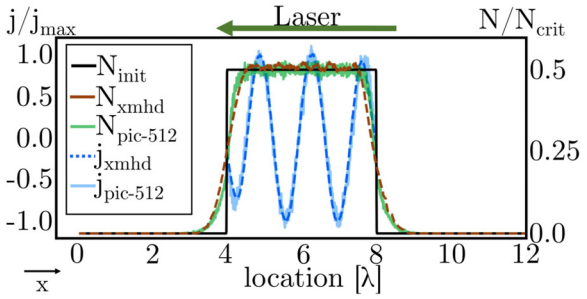

FIG. 2. A comparison at $t = 5.8$ ps of current density and electron number density from XMHD and OSIRIS simulations for a 1D *He* plasma initialized with $T_e = 1$ eV, $n_e/n_{crit} = 0.5$, $Z = 1$, $I_{laser} = 3.5 \times 10^{17}$ W/m^2, and $\lambda = 527$ nm. The collisional model was enabled within OSIRIS, and both PERSEUS and OSIRIS used a fixed Coulomb logarithm, $\ln\Lambda = 0.1$. The collisional model used in OSIRIS was that described by Perez *et al.*[34] The PIC domain used 512 particles-per-cell. Both simulations used heavily over-sampled cells with $\Delta x = \lambda/120$.

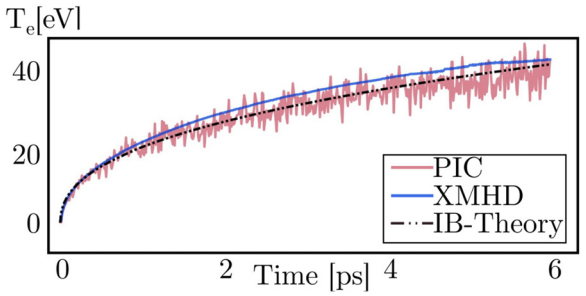

FIG. 4. A comparison at $t = 5.8$ ps of electron temperature, T_e, from XMHD and OSIRIS simulations for a 1D *He* plasma initialized with $T_e = 1$ eV, $n_e/n_{crit} = 0.5$, $Z = 1$, $I_{laser} = 3.5 \times 10^{17}$W/m^2, and $\lambda = 527$ nm. The collisional model was enabled within OSIRIS, and both PERSEUS and OSIRIS used a fixed Coulomb logarithm, $\ln\Lambda = 0.1$. The collisional model used in OSIRIS was that described by Perez *et al.*[34] The PIC domain used 512 particles-per-cell. Both simulations used heavily over-sampled cells with $\Delta x = \lambda/120$.

simulations. XMHD resistivity, η, was artificially set to approach a low-collisionality regime such that the electron inertia terms in Eq. (1) dominate over the Ohmic ones, $\eta \ll (\frac{1}{\omega_{pe} t_0})^3$. This is where PIC codes like OSIRIS have been validated. The output is taken approximately 5.8 ps into the simulation, where we see that not only does j look identical for both models, but n_e is also remarkably close. Similar agreement was observed for the electric and magnetic fields.

Since both XMHD and PIC models include collisions for simulations shown in Fig. 2, it is useful to directly compare thermal energy transfer between these two methods. The electron particle distribution function was sampled in the simulation domain ($x = 6\lambda$) and fitted with a Maxwell–Boltzmann curve to calculate the electron temperature T_e. The velocity phase space in Fig. 3 shows the distribution function line-out in blue, the fit in solid red, and the initial (1 eV) distribution in black. Figure 4 shows T_e matches well between these two computational methods over the course of the entire simulation. The black *IB-theory* curve indicates the expected plasma temperature assuming all the absorbed laser energy follows an inverse bremsstrahlung process and is directly converted to thermal energy. This analytic absorption model will also be discussed later using Eqs. (7) and (8).

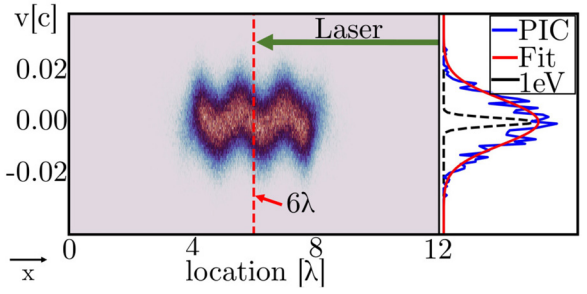

FIG. 3. (left) The electron velocity-position phase-space from OSIRIS. The velocity-axis represents the simulation's z-direction, which is aligned with the electric field of the laser. The location axis represents the simulation's x-direction, which is the propagation direction of the laser. (right) A line-out from x=6λ of the electron distribution function. This 6λ line-out location is indicated by the dotted red line. The solid red and blue curves represent the fitted and raw distribution functions, respectively. Also indicated in black is the initial 1 eV distribution function for the plasma.

Table I shows that while XMHD had performance gains in the collisionless regime ($\ln\Lambda = 0$), the real advantage of PERSEUS happens when collisions were introduced ($\ln\Lambda = 0.1$). For simulations with $\ln\Lambda = 0.1$ and particle counts of 128 and 512, PERSEUS demonstrated improvement factors ranging from 2.1 to 7.4. PERSEUS is particularly efficient in hot and dense collisional conditions, which requires a high number of particles to sample the phase-space.

Since collisional models are distinct from a native PIC algorithm, the combination can cause additional numerical considerations,[69] such as numerical heating[70] and cooling.[71] This can lead to particle-per-cell requirements even into the thousands,[71] which Table I suggests would lead to a more than 20× increase in computational time over PERSEUS.

We have so far demonstrated compatibility with ray-tracing models as well as a remarkable similarity in late-time simulations with PIC. So we now present and discuss the mechanisms that lead to collisional energy transfer in XMHD.

COLLISIONAL ABSORPTION IN LPI

This work will now focus on an under-dense regime, as this allows us to investigate both the resonance in Eq. (4) and collisional absorption within a single domain. Since XMHD agrees with PIC for long time durations, we focus here on shorter times to catch the

TABLE I. Performance comparison of OSIRIS and PERSEUS runs. The simulations were identical between the two codes, with the exception of the particle count and the $\ln\Lambda$, which was varied as indicated above. The *worsening factor* indicates the runtime multiplier relative to XMHD.

	$\ln\Lambda$	# Particles	TCycles	Cycles/particle	Worsening factor
OSIRIS	0.0	8192	5530	675	33.0
OSIRIS	0.0	512	347	678	2.1
OSIRIS	0.0	128	89.7	701	0.5
OSIRIS	0.1	512	1240	2410	7.4
OSIRIS	0.1	128	352	2750	2.1
PERSEUS	0.1		168		1.0

transient regime where the laser energy is transferred to the plasma. Additionally, since the plasma response can lead to additional electromagnetic waves, results are shown from both a continuous laser and one with 6-periods only. The latter allows us to observe re-emitted waves.

Although we restrict this work to fluid-like resistivity and distribution functions, the Spitzer model generally needs to be modified for high- and low-frequency lasers,[26] as well as for varying ionization states[72] and densities.[73] To maintain validity of the fluid model, the Langdon parameter[74,75] here is $\alpha \approx 1$, which keeps error from super-Gaussianity relatively low.[76]

Figure 5 shows the electric field (E_z) computed by the code in an initially isotropic under-dense step-density plasma. This field is primarily composed of electron inertia ($\frac{\partial \mathbf{j}}{\partial t}$) and the Ohmic heating. Initially, displacement currents dominate inside the low-density/vacuum portion of the plasma domain. Then physical currents take over as the density is large enough to supply electrons easily. Although this would not be a surprising result for a purely explicit 2-fluid code, we see that our semi-implicit 1-fluid (2-energy) XMHD formulation also captures this interaction.

While there is collisional momentum transfer between ions and electrons, a detailed analysis found it relatively insignificant from the electron perspective. So, the dominant energy exchange in LPIs is best described by considering Poynting's theorem

$$\frac{\mathrm{d}}{\mathrm{dt}}(u_E + u_B) + \nabla \cdot \mathbf{S} = -\mathbf{j} \cdot \mathbf{E}, \tag{5}$$

where $\mathbf{S}$ is the Poynting flux and u_E and u_B are the electric and magnetic energy densities, respectively. The heating term on the RHS only gets turned into $\mathbf{E} \cdot \mathbf{j} \approx \eta j^2$ when $\mathbf{E} \approx \eta \mathbf{j}$. However, the Ohmic term in Eq. (1) does not dominate the electric field in an under-dense plasma (see Fig. 5). Instead, Fig. 6 shows the laser field heats the plasma by resonance of Eq. (4), forcing oscillatory kinetic energy into the electron fluid. This energy is then quickly thermalized through resistive collisions.

The inset plot in Fig. 6 shows the plasma first gains kinetic energy before resistivity initiates energy transfer. Under these assumptions, the plasma behaves as an RLC circuit. The oscillatory motion stores reactive energy, while the collisional energy corresponds to dissipation. When the 6-period laser turns off, the remaining reactive oscillatory energy smoothly turns into thermal energy. $[\mathbf{E} \cdot \mathbf{j}]_{\text{reactive}} \approx \frac{m_e}{e^2 N_e} j \frac{\partial j}{\partial t} = \frac{\partial}{\partial t} \frac{\rho_e v_e^2}{2}$ is just the kinetic energy given to the electron fluid by the laser. If $\ln \Lambda$ is allowed to vary, then the plasma can store much more

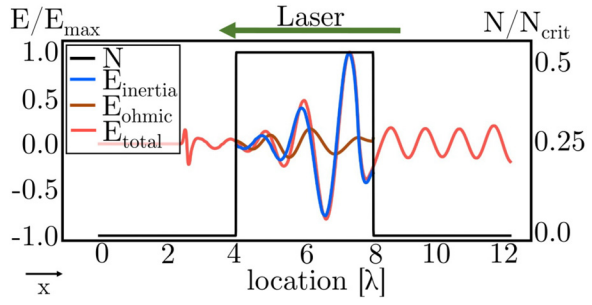

FIG. 5. The electric field E_z output from the simulation compared to the components computed from Generalized Ohm's law. Also plotted is the N_{ion} to show the validity across a plasma–vacuum interface.

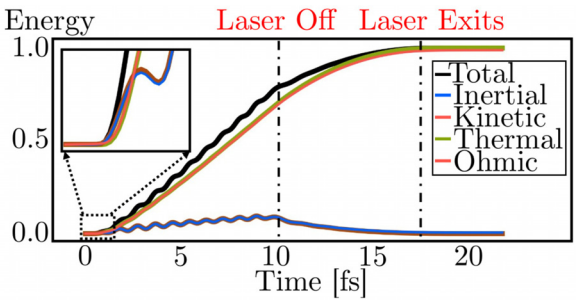

FIG. 6. The main cumulative contributions of the energy equation for electron fluids computed using $\mathbf{E} \cdot \mathbf{j}$. Also shown is the instantaneous partition of energy for electron fluid as a sum of thermal ($k_b T$) and directed kinetic ($\frac{1}{2} m v^2$). The geometry here is a wedge-density profile pre-heated to 1 eV and with constant $\ln \Lambda = 1$. The laser intensity is $S = 3.5 \times 10^{17} \mathrm{W/m^2}$ ($a_0 \approx 0.003$).

oscillatory energy as the increase in temperature lowers $\ln \Lambda$ and thereby reduces η and increases the current density.

Since inverse bremsstrahlung is used in most MHD codes as the primary laser–plasma interaction model, we now show the work presented so far does capture IB absorption. In this context, the basic analytic theory[1,77,78] gives the following dispersion relation:

$$\omega^2 = k^2 c^2 + \omega_{pe}^2 - i \frac{\omega \omega_{pe}^2}{\nu_{ei}}, \tag{6}$$

and it shows that lasers have their electromagnetic waves damped at a rate $k_{ib} = \nu_{ei} \omega_{pe}^2 / \mu c \omega^2$, in the limit of low laser intensity, $\mathbf{S}$. Thus, the laser intensity decays as $dS/dx = -k_{ib} S$ with a corresponding solution, $\mathbf{S} = \mathbf{S}_0 e^{-ax} \sin(bx + c)$. μ is the real refractive index and k_{ib} is the inverse bremsstrahlung coefficient.

Using a continuous low-intensity laser, Fig. 7(a) shows the Poynting flux, $\mathbf{S}_{\text{xmhd}}$, computed directly from XMHD outputs along with the damped exponential function, $\mathbf{S}_{T_{min/max}}$, with constants matching the IB theory from Eq. (6). However, a choice of what rapidly varying T_e to use must be made when computing ν_{ei}. The color and spatial location of the solid circles show values and location used for corresponding curves, $\mathbf{S}_{T_{min}}$ and $\mathbf{S}_{T_{max}}$. Although the match is nearly perfect for one choice of T_e, for a higher laser intensity lasers, such as what is shown in Fig. 7(b), this is not necessarily true. Figure 5 along with Eq. (5) show that since the electric field in the plasma is primarily composed of electron inertia for the first few wavelengths, then this leads to an increase in reactive kinetic energy over thermal kinetic energy. This can be seen in Fig. 7(b), where T_e rapidly increases in the more intense laser field. Consequently, $\eta \propto T^{-3/2}$ becomes low enough to nearly stop collisional absorption altogether. Instead, energy is pumped into the directed kinetic energy of the plasma, where it shows up as an electron current, $\mathbf{j}_L$. Figure 7(b) shows this effect as the E_k/E_T (ratio of directed-kinetic to total energy) curve increases relative to Fig. 7(a). Since Eq. (6) requires immediate thermalization of laser-deposited energy, then its solution is no longer compatible with the system. Because the energy is retained as directed kinetic energy, dynamics associated with $\mathbf{j}_L \times \mathbf{B}$ can now potentially takeover. This is a clear departure from IB theory.

To isolate incoming laser from the reflected/excited waves we now turn to results using only a 6-period input laser. Now there is a definite "laser-off" portion, which shows how energy is partitioned

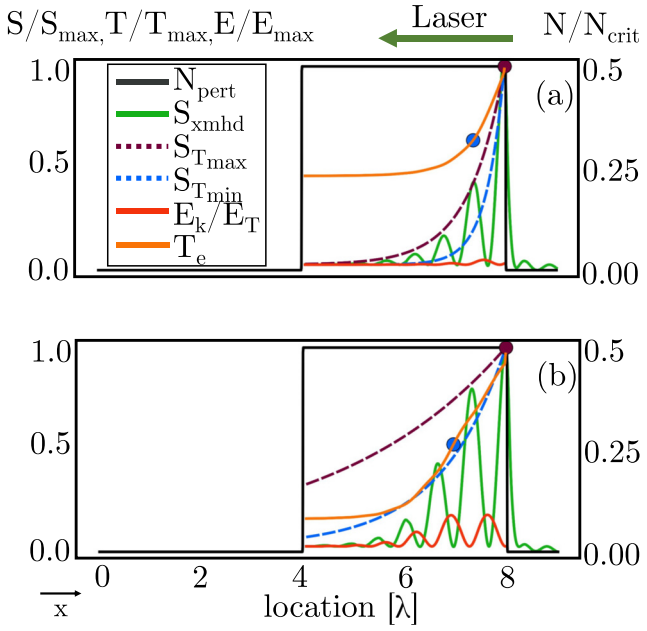

FIG. 7. The scaling factor between a basic inverse bremsstrahlung model and the predictions from an XMHD model for two different laser powers with a plasma pre-heated to 1 eV (to ensure ionization) (a) $\mathbf{S} = 7.5 \times 10^{16}$ and (b) $\mathbf{S} = 7.5 \times 10^{17}$ W/m^2. $\mathbf{S}$ refers to the Poynting flux, with the green curve computed from XMHD outputs, the dotted lines computed from analytic IB theory at two different temperatures, whose location in the plasma is shown in the filled-in circles. The vertical axes are all unitless and refer to the fraction of maximum value for each quantity, except the density, which is the fraction of critical density. Additionally, the red curve shows the fraction of directed kinetic energy ($\frac{E_k}{E_T}$) in the system relative to the total energy (including thermal).

among the electron fluid. Similar to an approach in an earlier work,[79] we computed the edge-temperature using a 1D method. After integrating the electron energy equation, Eq. (7), we get T_e as a function of the laser fluence, Φ, shown in Eq. (8).

$$\frac{3}{2} n_e k_b \frac{\partial T_e}{\partial t} = \frac{\kappa}{T_e^{3/2}} S, \tag{7}$$

$$T_e(x = 0, t) = \left(\frac{5}{3} \frac{\kappa}{n_e k_b} \Phi_0 + T_{e0}^{5/2} \right)^{2/5}. \tag{8}$$

This method assumes constant Coulomb logarithm ($\ln \Lambda$), Spitzer-like collisions, no thermal conduction, and immobile ions. This first assumption may not be particularly valid, since when temperature increases, $\ln \Lambda$ can also vary significantly. In our simulations $\ln \Lambda$ falls between 0 and 3, so we chose a constant value of 1.

Figure 8 shows there is a good agreement of the edge-temperature at the plasma-vacuum region when plotting the value from Eq. (8) (using the laser poynting flux, S) along with the actual rise in temperature produced by the simulation, indicating XMHD captures IB relatively well.

The spatial shape of T_e is different from the analytic theory because electron inertia implies a time lag. This along with Spitzer resistivity, which is ultimately velocity-based, implies there is an inherent time required to pump energy into electron oscillations before they can thermalize it.

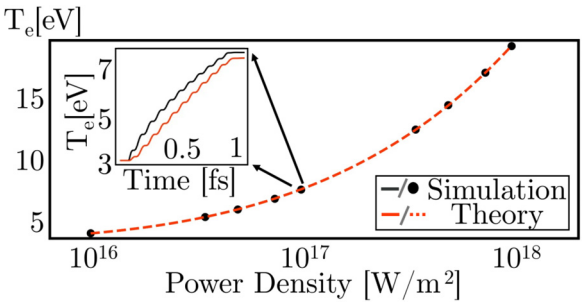

FIG. 8. Comparison between the final incident edge electron-temperature as predicted by a simplified inverse bremsstrahlung calculation from a pulsed laser and the measurement from simulation using a wedge-density profile pre-heated to 1 eV. The dotted red line shows a fit of the data to a polynomial form predicted by IB theory from Eq. (8) $(ax + b)^c$. The black dots represent the final temperature for individual simulation predictions for a laser power density specified on the x-axis. The inset plot shows an example edge temperature evolution for the simulation in black vs theory in red.

CONCLUSIONS

This paper explores how XMHD can be used to study the intricacies of collisional LPI across a broad range of parameters, which remains elusive to particle-in-cell and MHD models. It also demonstrates compatibility with both ray-tracing and particle-in-cell methods within their realms of validity. While this work explores fundamental effects that are well understood, it does it by using a completely different approach. Leveraging the GOL, this work demonstrates XMHD can capture the oscillatory nature of the electrons and shows how the plasma frequency naturally arises in the proposed framework. We have shown that LPI appears as a mix of reactance, via resonance, and dissipation, via resistivity. The reactive component stems from harmonic oscillations, which stores mechanical energy inside the electron motion. This is only possible because electrons have a non-zero mass in our model. The model can recover many fundamental aspects of LPI usually captured by particle-in-cell or multi-fluid MHD codes, such as reflection, absorption, and even a critical density. Energy transfer and its subsequent decay match well analytic theory for simple configurations, and at low energies. Because of its accuracy, XMHD is appropriate for regimes that can be too expensive to simulate with multi-fluid codes and that MHD cannot capture.

Since XMHD accounts for the entire $d\mathbf{j}/dt = \partial \mathbf{j}/\partial t + \mathbf{v} \cdot \nabla \mathbf{j}$, this framework naturally bridges the gap between the kinetic and hydrodynamics scales. It also ensures computational continuity between the short scales, dominated by electron physics, and the large scale, dominated by ion dynamics. As a result, the effects of microscopic physics and their impact on macroscopic scales can be done by using the same code. Under such assumptions, using one code to compute LPI and how they impact plasma dynamics on larger scales is clearly possible and will be explored in the future work.

ACKNOWLEDGMENTS

This research was supported by the NSF CAREER Award No. PHY-1943939, the U.S. Department of Energy Center No. DE-NA0004148, and the Laboratory for Laser Energetics Horton Fellowships. We would also like to thank Professor Charlie Seyler for his invaluable guidance working with PERSEUS.

AUTHOR DECLARATIONS

Conflict of Interest

The authors have no conflicts to disclose.

Author Contributions

James R. Young: Conceptualization (equal); Data curation (equal); Formal analysis (equal); Investigation (equal); Methodology (equal); Resources (equal); Software (equal); Validation (equal); Visualization (equal); Writing – original draft (equal); Writing – review & editing (equal). **Pierre-Alexandre Gourdain:** Conceptualization (equal); Funding acquisition (equal); Methodology (equal); Project administration (equal); Resources (equal); Software (equal); Supervision (equal); Writing – review & editing (equal).

DATA AVAILABILITY

The data that support the findings of this study are available from the corresponding author upon reasonable request.

REFERENCES

[1]W. L. Kruer, *The Physics of Laser Plasma Interactions* (Addison, Wesley, 1988).
[2]B. Bezzerides, H. X. Vu, and J. M. Wallace, "Convective gain of stimulated Brillouin scattering in long-scale length, two-ion-component plasmas," Phys. Plasmas **3**, 1073–1090 (1996).
[3]V. V. Eliseev, W. Rozmus, V. T. Tikhonchuk, and C. E. Capjack, "Stimulated Brillouin scattering and ponderomotive self-focusing from a single laser hot spot," Phys. Plasmas **2**, 1712–1724 (1995).
[4]S. Hüller, G. Raj, W. Rozmus, and D. Pesme, "Crossed beam energy transfer in the presence of laser speckle ponderomotive self-focusing and nonlinear sound waves," Phys. Plasmas **27**, 022703 (2020).
[5]A. Ruocco, "Modelling of ponderomotive laser self-focusing in a plasma with a hydrodynamic code in the context of direct-drive inertial confinement fusion," Ph.D. thesis (Université de Bordeaux, 2020).
[6]O. M. Gradov and L. Stenflo, "Magnetic-field generation by a finite-radius electromagnetic beam," Phys. Lett. A **95**, 233–234 (1983).
[7]N. Shukla, P. K. Shukla, and L. Stenflo, "Magnetization of a warm plasma by the nonstationary ponderomotive force of an electromagnetic wave," Phys. Rev. E **80**, 027401 (2009).
[8]V. V. Ivanov, A. V. Maximov, R. Betti, L. S. Leal, J. D. Moody, K. J. Swanson, and N. A. Huerta, "Generation of strong magnetic fields for magnetized plasma experiments at the 1-MA pulsed power machine," Matter Radiat. Extremes **6**, 046901 (2021).
[9]D. M. Palmer, S. Barthelmy, N. Gehrels, R. M. Kippen, T. Cayton, C. Kouveliotou, D. Eichler, R. A. M. J. Wijers, P. M. Woods, J. Granot, Y. E. Lyubarsky, E. Ramirez-Ruiz, L. Barbier, M. Chester, J. Cummings, E. E. Fenimore, M. H. Finger, B. M. Gaensler, D. Hullinger, H. Krimm, C. B. Markwardt, J. A. Nousek, A. Parsons, S. Patel, T. Sakamoto, G. Sato, M. Suzuki, and J. Tueller, "A giant γ-ray flare from the magnetar SGR 1806-20," Nature **434**, 1107–1109 (2005).
[10]S. Jordan, R. Aznar Cuadrado, R. Napiwotzki, H. M. Schmid, and S. K. Solanki, "The fraction of DA white dwarfs with kilo-Gauss magnetic fields," Astron. Astrophys. **462**, 1097–1101 (2007).
[11]E. Sobacchi, Y. Lyubarsky, A. M. Beloborodov, L. Sironi, and M. Iwamoto, "Saturation of the filamentation instability and dispersion measure of fast radio bursts," Astrophys. J. Lett. **943**, L21 (2023).
[12]A. Ghosh, D. Kagan, U. Keshet, and Y. Lyubarsky, "Nonlinear electromagnetic-wave interactions in pair plasma. I. Nonrelativistic regime," Astrophys. J. **930**, 106 (2022).
[13]P. Kaw, G. Schmidt, and T. Wilcox, "Filamentation and trapping of electromagnetic radiation in plasmas," Phys. Fluids **16**, 1522 (1973).
[14]V. Del Pizzo, B. Luther-Davies, and M. R. Siegrist, "Self-focussing of a laser beam in a multiply ionized, absorbing plasma," Appl. Phys. **18**, 199–204 (1979).
[15]K. G. Estabrook, E. J. Valeo, and W. L. Kruer, "Two-dimensional relativistic simulations of resonance absorption," Phys. Fluids **18**, 1151 (1975).
[16]R. Dragila and J. Krepelka, "Laser plasma density profile modification by ponderomotive force," J. Phys. **39**, 617–623 (1978).
[17]J. R. Smith, C. Orban, G. K. Ngirmang, J. T. Morrison, K. M. George, E. A. Chowdhury, and W. M. Roquemore, "Particle-in-cell simulations of density peak formation and ion heating from short pulse laser-driven ponderomotive steepening," Phys. Plasmas **26**, 123103 (2019).
[18]G. Lehmann and K. H. Spatschek, "Plasma photonic crystal growth in the trapping regime," Phys. Plasmas **26**, 013106 (2019).
[19]Z.-M. Sheng, J. Zhang, and D. Umstadter, "Plasma density gratings induced by intersecting laser pulses in underdense plasmas," Appl. Phys. B **77**, 673–680 (2003).
[20]L. Plaja and L. Roso, "Analytical description of a plasma diffraction grating induced by two crossed laser beams," Phys. Rev. E **56**, 7142–7146 (1997).
[21]M. R. Edwards and P. Michel, "Plasma transmission gratings for compression of high-intensity laser pulses," Phys. Rev. Appl. **18**, 024026 (2022).
[22]M. R. Edwards, S. Waczynski, E. Rockafellow, L. Manzo, A. Zingale, P. Michel, and H. M. Milchberg, "Control of intense light with avalanche-ionization plasma gratings," Optica **10**, 1587 (2023).
[23]L. Shi, W. Li, Y. Wang, X. Lu, L. Ding, and H. Zeng, "Generation of high-density electrons based on plasma grating induced Bragg diffraction in air," Phys. Rev. Lett. **107**, 095004 (2011).
[24]H. Peng, C. Riconda, M. Grech, C.-T. Zhou, and S. Weber, "Dynamical aspects of plasma gratings driven by a static ponderomotive potential," Plasma Phys. Controlled Fusion **62**, 115015 (2020).
[25]H. Peng, C. Riconda, M. Grech, J.-Q. Su, and S. Weber, "Nonlinear dynamics of laser-generated ion-plasma gratings: A unified description," Phys. Rev. E **100**, 061201 (2019).
[26]J. Dawson and C. Oberman, "High-frequency conductivity and the emission and absorption coefficients of a fully ionized plasma," Phys. Fluids **5**, 517–524 (1962).
[27]R. Hockney and J. Eastwood, *Computer Simulations Using Particles* (McGraw-Hill, 1981).
[28]T. B. Kaiser, "Laser ray tracing and power deposition on an unstructured three-dimensional grid," Phys. Rev. E **61**, 895–905 (2000).
[29]A. Colaïtis, I. Igumenshchev, J. Mathiaud, and V. Goncharov, "Inverse ray tracing on icosahedral tetrahedron grids for non-linear laser plasma interaction coupled to 3D radiation hydrodynamics," J. Comput. Phys. **443**, 110537 (2021).
[30]T. Takizuka and H. Abe, "A binary collision model for plasma simulation with a particle code," J. Comput. Phys. **25**, 205–219 (1977).
[31]Y. Sentoku, K. Mima, Y. Kishimoto, and M. Honda, "Effects of relativistic binary collisions on PIC simulation of laser plasmas," J. Phys. Soc. Jpn. **67**, 4084–4088 (1998).
[32]Y. Sentoku and A. Kemp, "Numerical methods for particle simulations at extreme densities and temperatures: Weighted particles, relativistic collisions and reduced currents," J. Comput. Phys. **227**, 6846–6861 (2008).
[33]K. Nanbu and S. Yonemura, "Weighted particles in Coulomb collision simulations based on the theory of a cumulative scattering angle," J. Comput. Phys. **145**, 639–654 (1998).
[34]F. Pérez, L. Gremillet, A. Decoster, M. Drouin, and E. Lefebvre, "Improved modeling of relativistic collisions and collisional ionization in particle-in-cell codes," Phys. Plasmas **19**, 083104 (2012).
[35]D. P. Higginson, I. Holod, and A. Link, "A corrected method for Coulomb scattering in arbitrarily weighted particle-in-cell plasma simulations," J. Comput. Phys. **413**, 109450 (2020).
[36]B. I. Cohen, A. M. Dimits, and D. J. Strozzi, "A grid-based binary model for Coulomb collisions in plasmas," J. Comput. Phys. **234**, 33–43 (2013).
[37]S. Braginskii, "Transport processes in a plasma," Rev. Plasma Phys. **1**, 205 (1965).
[38]B. Fryxell, K. Olson, P. Ricker, F. X. Timmes, M. Zingale, D. Q. Lamb, P. MacNeice, R. Rosner, J. W. Truran, and H. Tufo, "FLASH: An adaptive mesh hydrodynamics code for modeling astrophysical thermonuclear flashes," Astrophys. J. Suppl. Ser. **131**, 273–334 (2000).
[39]J. Delettrez, R. Epstein, M. C. Richardson, P. A. Jaanimagi, and B. L. Henke, "Effect of laser illumination nonuniformity on the analysis of time-resolved x-ray measurements in uv spherical transport experiments," Phys. Rev. A **36**, 3926–3934 (1987).

[40]D. Keller, T. J. B. Collins, J. A. Delettrez, P. W. McKenty, P. B. Radha, R. P. J. Town, B. Whitney, and G. A. Moses, "Draco—A new multidimensional hydrocode," Poster session BP1.39, presented at the 41st APS, Seattle, WA, 15 November 1999. https://flux.aps.org/meetings/YR99/DPP99/abs/S175039.html.
[41]M. M. Marinak, R. E. Tipton, O. L. Landen, T. J. Murphy, P. Amendt, S. W. Haan, S. P. Hatchett, C. J. Keane, R. McEachern, and R. Wallace, "Three-dimensional simulations of Nova high growth factor capsule implosion experiments," Phys. Plasmas **3**, 2070–2076 (1996).
[42]T. H. Stix, *Waves in Plasmas* (Springer Science & Business Media, 1992).
[43]F. Holderied, S. Possanner, and X. Wang, "MHD-kinetic hybrid code based on structure-preserving finite elements with particles-in-cell," J. Comput. Phys. **433**, 110143 (2021).
[44]J. R. Young, M. B. Adams, H. Hasson, I. West-Abdallah, M. Evans, and P.-A. Gourdain, "Using extended MHD to explore lasers as a trigger for x-pinches," Phys. Plasmas **28**, 102703 (2021).
[45]R. V. Shapovalov, R. B. Spielman, and G. R. Imel, "An oil-free compact X-pinch plasma radiation source: Design and radiation performance," Rev. Sci. Instrum. **88**, 063504 (2017).
[46]R. Shapovalov, M. Adams, M. Evans, H. Hasson, J. Young, I. West-Abdallah, and P.-A. Gourdain, "Low-inductance load test of a new 250-Ka, 150-Ns pulser for fast X-pinch sources," in *IEEE Pulsed Power & Plasma Science (PPPS)* (IEEE, Orlando, FL, 2019).
[47]F. Zucchini, S. N. Bland, C. Chauvin, P. Combes, D. Sol, A. Loyen, B. Roques, and J. Grunenwald, "Characteristics of a molybdenum x-pinch x-ray source as a probe source for x-ray diffraction studies," Rev. Sci. Instrum. **86**, 033507 (2015).
[48]J. Strucka, J. Halliday, T. Gheorghiu, H. Horton, B. Krawczyk, P. Moloney, S. Parker, G. Rowland, N. Schwartz, S. Stanislaus *et al.*, "A portable X-pinch design for x-ray diagnostics of warm dense matter," Matter Radiat. Extremes **7**, 016901 (2022).
[49]R. K. Follett, J. G. Shaw, J. F. Myatt, V. N. Goncharov, D. H. Edgell, D. H. Froula, and J. P. Palastro, "Ray-based modeling of cross-beam energy transfer at caustics," Phys. Rev. E **98**, 043202 (2018).
[50]J. E. Harvey, R. G. Irvin, and R. N. Pfisterer, "Modeling physical optics phenomena by complex ray tracing," Opt. Eng. **54**, 035105 (2015).
[51]D. E. Hinkel-Lipsker, B. D. Fried, and G. J. Morales, "Analytic expression for mode conversion of Langmuir and electromagnetic waves," Phys. Rev. Lett. **62**, 2680–2682 (1989).
[52]P. Michel, *Introduction to Laser-Plasma Interactions*, Graduate Texts in Physics (Springer, Cham, 2023).
[53]J. P. Freidberg, R. W. Mitchell, R. L. Morse, and L. I. Rudsinski, "Resonant absorption of laser light by plasma targets," Phys. Rev. Lett. **28**, 795–799 (1972).
[54]J. P. Palastro, J. G. Shaw, R. K. Follett, A. Colaïtis, D. Turnbull, A. V. Maximov, V. N. Goncharov, and D. H. Froula, "Resonance absorption of a broadband laser pulse," Phys. Plasmas **25**, 123104 (2018).
[55]J. R. Davies, D. H. Barnak, R. Betti, E. M. Campbell, P.-Y. Chang, A. B. Sefkow, K. J. Peterson, D. B. Sinars, and M. R. Weis, "Laser-driven magnetized liner inertial fusion," Phys. Plasmas **24**, 062701 (2017).
[56]E. C. Hansen, D. H. Barnak, R. Betti, E. M. Campbell, P.-Y. Chang, J. R. Davies, V. Y. Glebov, J. P. Knauer, J. Peebles, S. P. Regan, and A. B. Sefkow, "Measuring implosion velocities in experiments and simulations of laser-driven cylindrical implosions on the OMEGA laser," Plasma Phys. Controlled Fusion **60**, 054014 (2018).
[57]C. E. Seyler and M. R. Martin, "Relaxation model for extended magnetohydrodynamics: Comparison to magnetohydrodynamics for dense Z-pinches," Phys. Plasmas **18**, 012703 (2011).
[58]M. R. Martin, "Generalized Ohm's law at the plasma-vacuum interface," Ph.D. thesis (Cornell University, 2010).
[59]N. D. Hamlin and C. E. Seyler, "Relativistic modeling capabilities in PERSEUS extended-MHD simulation code for HED plasmas," IEEE Trans. Plasma Sci. **44**, 1112–1126 (2016).
[60]P.-A. Gourdain, "The impact of the Hall term on tokamak plasmas," arXiv:1703.00987 [physics] (2017).
[61]S. Chapman and T. G. Cowling, *The Mathematical Theory of Non-Uniform Gases: An Account of the Kinetic Theory of Viscosity, Thermal Conduction and Diffusion in Gases* (Cambridge University Press, 1990).
[62]*Reconnection of Magnetic Fields: Magnetohydrodynamics and Collisionless Theory and Observations*, edited by J. Birn and E. R. Priest (Cambridge University Press, Cambridge, 2007).
[63]J. F. Drake, D. Biskamp, and A. Zeiler, "Breakup of the electron current layer during 3-D collisionless magnetic reconnection," Geophys. Res. Lett. **24**, 2921–2924, https://doi.org/10.1029/97GL52961 (1997).
[64]S. T. Jones and S. E. Parker, "Including electron inertia without advancing electron flow," J. Comput. Phys. **191**, 322–327 (2003).
[65]P. A. Muñoz, N. Jain, P. Kilian, and J. Büchner, "A new hybrid code (CHIEF) implementing the inertial electron fluid equation without approximation," Comput. Phys. Commun. **224**, 245–264 (2018).
[66]M. M. Kuznetsova, M. Hesse, and D. Winske, "Kinetic quasi-viscous and bulk flow inertia effects in collisionless magnetotail reconnection," J. Geophys. Res. Space Phys. **103**, 199–213, https://doi.org/10.1029/97JA02699 (1998).
[67]R. G. Hemker, "Particle-in-cell modeling of plasma-based accelerators in two and three dimensions," arXiv:1503.00276 (2015).
[68]G. Lapenta, "Exactly energy conserving semi-implicit particle in cell formulation," J. Comput. Phys. **334**, 349–366 (2017).
[69]J. R. Angus, A. Link, A. Friedman, D. Ghosh, and J. D. Johnson, "On numerical energy conservation for an implicit particle-in-cell method coupled with a binary Monte-Carlo algorithm for Coulomb collisions," J. Comput. Phys. **456**, 111030 (2022).
[70]E. P. Alves, W. B. Mori, and F. Fiuza, "Numerical heating in particle-in-cell simulations with Monte Carlo binary collisions," Phys. Rev. E **103**, 013306 (2021).
[71]J. R. Angus, A. J. Link, and A. E. Schmidt, "1D kinetic study of pinch formation in a dense plasma focus: Transition from collisional to collisionless regimes," Phys. Plasmas **28**, 010701 (2021).
[72]S. Skupsky, "'Coulomb logarithm' for inverse-bremsstrahlung laser absorption," Phys. Rev. A **36**, 5701–5712 (1987).
[73]Y. T. Lee and R. M. More, "An electron conductivity model for dense plasmas," Phys. Fluids **27**, 1273 (1984).
[74]A. B. Langdon, "Nonlinear inverse bremsstrahlung and heated-electron distributions," Phys. Rev. Lett. **44**, 575–579 (1980).
[75]D. Turnbull, A. Colaïtis, A. M. Hansen, A. L. Milder, J. P. Palastro, J. Katz, C. Dorrer, B. E. Kruschwitz, D. J. Strozzi, and D. H. Froula, "Impact of the Langdon effect on crossed-beam energy transfer," Nat. Phys. **16**, 181–185 (2020).
[76]C. D. Decker, W. B. Mori, J. M. Dawson, and T. Katsouleas, "Nonlinear collisional absorption in laser-driven plasmas," Phys. Plasmas **1**, 4043–4049 (1994).
[77]A. M. M. Schiavi, "Study of laser produced plasmas by X-ray and proton radiography," Ph.D. thesis (Imperial College London, 2004).
[78]T. W. Johnston and J. M. Dawson, "Correct values for high-frequency power absorption by inverse bremsstrahlung in plasmas," Phys. Fluids **16**, 722 (1973).
[79]J. Denavit and D. W. Phillion, "Laser ionization and heating of gas targets for long-scale-length instability experiments," Phys. Plasmas **1**, 1971–1984 (1994).